TU Delft

Delft University of Technology

The potential of transparent sputtered NaI:Tm^{2+}, $CaBr_2$:Tm^{2+}, and CaI_2:Tm^{2+} thin films as luminescent solar concentrators

Merkx, Evert P.J.; Plokker, Maarten P.; van der Kolk, Erik

DOI
10.1016/j.solmat.2020.110944

Publication date
2021

Document Version
Final published version

Published in
Solar Energy Materials and Solar Cells

Citation (APA)
Merkx, E. P. J., Plokker, M. P., & van der Kolk, E. (2021). The potential of transparent sputtered NaI:Tm^{2+}, $CaBr_2$:Tm^{2+}, and CaI_2:Tm^{2+} thin films as luminescent solar concentrators. *Solar Energy Materials and Solar Cells, 223*, Article 110944. https://doi.org/10.1016/j.solmat.2020.110944

Important note
To cite this publication, please use the final published version (if applicable).
Please check the document version above.

Copyright
Other than for strictly personal use, it is not permitted to download, forward or distribute the text or part of it, without the consent of the author(s) and/or copyright holder(s), unless the work is under an open content license such as Creative Commons.

Takedown policy
Please contact us and provide details if you believe this document breaches copyrights.
We will remove access to the work immediately and investigate your claim.

This work is downloaded from Delft University of Technology.
For technical reasons the number of authors shown on this cover page is limited to a maximum of 10.

Solar Energy Materials & Solar Cells 223 (2021) 110944

Contents lists available at ScienceDirect

Solar Energy Materials and Solar Cells

journal homepage: www.elsevier.com/locate/solmat

The potential of transparent sputtered NaI:Tm^{2+}, $CaBr_2$:Tm^{2+}, and CaI_2:Tm^{2+} thin films as luminescent solar concentrators

Evert P.J. Merkx *, Maarten P. Plokker, Erik van der Kolk

Luminescence Materials, Delft University of Technology, Mekelweg 15, 2629 JB, Delft, Netherlands

ARTICLE INFO

Keywords:
Building-integrated photovoltaics
Luminescent solar concentrator
Halide
Combinatorial science
Sputter deposition
Optical simulation

ABSTRACT

The parameters governing the performance of a luminescent solar concentrator (LSC) are determined for sputtered thin-films of NaI:Tm^{2+}, $CaBr_2$:Tm^{2+}, and CaI_2:Tm^{2+}. These parameters are determined by using six gradient thin film material libraries, combinatorially sputtered from metallic and pressed powder targets. These films show strong $4f^{13} \rightarrow 4f^{12}d^1$ absorption of maximally 752 cm^{-1} at.%$^{-1}$ for NaI:Tm^{2+}, 31 cm^{-1} at.%$^{-1}$ for $CaBr_2$:Tm^{2+}, and 473 cm^{-1} at.%$^{-1}$ for CaI_2:Tm^{2+}. This absorption covers the entire visible spectrum and does not overlap with the infrared 4f-4f emission at 1140 nm. Decay measurements are used to estimate the quantum yields of the thin-films. These quantum yields can be as high as 44 % for NaI:Tm^{2+}, when doped with 0.3 at.% Tm. Even at doping percentages as low as 0.3 at.%, the films appear to show luminescence quenching. The concentration-dependent absorption and quantum yield are combined with the index of refraction, resolved from transmission measurements, to simulate the optical efficiency of a thin film Tm^{2+}-doped halide LSC. These simulations show that LSCs based on Tm^{2+} can display excellent color rendering indices of up to 99 %, and neutral color temperatures, between 4500 K and 6000 K. Under optimal conditions, thin-films constrained to a thickness of 10 μm and 80 % transmission of the visible spectrum, would be able to display optical efficiencies of 0.71 %. This optical efficiency compares favorably to the maximally achievable 3.5 % under these constraints. This efficiency is largely independent of the size of LSC itself.

1. Introduction

Luminescent solar concentrators (LSCs) are an electricity-generating replacement for window glass, commonly found in windows or facades. This type of energy-generating replacement for building materials is called building-integrated PV (BIPV). These LSCs generate electricity through a luminescent coating deposited on the window glass. This coating harvests a fraction of the incoming sunlight and converts this to luminescent light. This luminescence is isotropically emitted and therefore remains largely trapped between the coating and the window glass, due to total internal reflection. For a refractive index of n = 1.7, around 80 % of the emitted light remains trapped. The trapped light travels by total internal reflection to the edges of the window. At the edges, the light impinges on photovoltaic (PV) cells that face the perimeter of the window. The PV cells then convert the trapped light to electricity. Due to their electricity-generating capabilities, LSCs can become part of the building envelope to realize net-zero energy buildings, in line with goals of the European Union [1].

Much progress has already been made in the LSC community. With the advent of efficient non-toxic type-II quantum dots (QDs) that are cheap to fabricate at large scale [2], LSCs are on their way to becoming a part of the building envelope. A disadvantage of these QDs, however, is their non-uniform light absorption. These QDs typically have an absorption that shoots up towards lower wavelengths. At high QD concentrations, this non-uniform absorption of light can lead to a sepia-colored appearance of the room illuminated through the LSC [3,4]. Recent developments in ultraviolet- and infrared-absorbing dyes [5–7] have a good aesthetic appeal, as the visible spectrum passes through these dyes unaltered. However, neither of these types of dye can attain a high power-conversion efficiency: Ultraviolet-absorbing LSCs will not reach high power outputs due to the low amount of photons in the solar spectrum [3]. Infrared-absorbing dyes suffer from high levels of self-absorption when scaled up to large sizes [6,8].

Another class of LSC materials are rare-earth-doped film coatings on glassy waveguides [9,10]. A specific example of these are halides doped with divalent thulium (Tm^{2+}) [11–13]. An LSC made from glass with low absorption of near-infrared light, covered by a thin-film of Tm^{2+}-doped halides avoids the issue of sepia coloring, thanks to the almost uniform absorption of the Tm^{2+} across the visible spectrum. Furthermore, because Tm^{2+} absorbs visible light and emits infrared light, it does not suffer from any losses due to parasitic self-absorption

* Corresponding author.
E-mail address: e.p.j.merkx@tudelft.nl (E.P.J. Merkx).

https://doi.org/10.1016/j.solmat.2020.110944
Received 1 July 2020; Received in revised form 9 December 2020; Accepted 20 December 2020
Available online 13 January 2021
0927-0248/© 2020 The Authors. Published by Elsevier B.V. This is an open access article under the CC BY license (http://creativecommons.org/licenses/by/4.0/).

of its own emission. To efficiently convert this infrared emission to electricity, $CuInSe_2$ (CIS) solar cells can be used [12]. Some aspects of the performance of Tm_2^+-doped halides have been investigated in powder form [14–21]. Until now, a full study on the applicability of these Tm^{2+}-doped halides as a luminescent solar concentrator has not yet been undertaken. To evaluate the performance of these materials, we present a combinatorial study on the LSC characteristics of some of these Tm^{2+}-doped halides. A combinatorial sputtering approach is chosen, because this approach will yield all parameters relevant to modeling the performance of an LSC using only a few thin-film deposition steps, as will be elaborated on later. In this article, we will cover sputter-deposited thin-films of NaI, $CaBr_2$, and CaI_2 doped with a concentration gradient of Tm, applied directly on a glass waveguide.

The optical efficiency of an LSC, defined as the ratio of photons incident on the LSC surface to the photons emitted at the edge, is given by [8]

$$\eta_{opt} = (1 - R)\eta_{abs}\eta_{QY}\eta_{trap}\eta_{WG}\eta_{SA}. \quad (1)$$

Here, $1 - R$ is the fraction of incident light coupled into the LSC, η_{abs} is the fraction of light absorbed by the luminescent particles, η_{QY} is the photoluminescent quantum yield: the ratio of the number of photons absorbed by the luminescent particle, to the number of photons emitted; η_{trap} is the trapping efficiency, which gives the fraction of light that will remain in the LSC after conversion, through total internal reflection; η_{WG} is the efficiency of the waveguide, i.e., the fraction of light that will be lost during transport to the edges of the waveguide due to scattering effects. η_{SA} is the self-absorption efficiency. This factor takes into account how the efficiency is altered by having overlapping absorption and emission.

All parameters from Eq. (1) can be derived from measurements on a combinatorially sputtered model system. $(1 - R)\eta_{abs}\eta_{trap}$ is a function of the complex refractive index $\tilde{n}(\lambda) = n(\lambda) + ik(\lambda)$, with $n \equiv n(\lambda)$ the (real part of the) refractive index and $k \equiv k(\lambda)$ the extinction coefficient. k, in turn, is related to the molar absorption coefficient $\varepsilon(\lambda)$ through

$$\varepsilon(\lambda) = \frac{4\pi k(\lambda)}{\lambda c_{Tm}}. \quad (2)$$

Here, λ is the wavelength of light and c_{Tm} the concentration of the used dopant, Tm in our case.

η_{QY} is straightforward to determine when using diffuse phosphor powders. In the case of powders, one takes the ratio of integrated emission to integrated absorption of light from a known excitation source using integrating sphere measurements (see e.g., Ref. [22]). For luminescent thin-films, η_{QY} cannot be determined so directly, because of the influence of the waveguide. A way to overcome this difficulty is by measuring the mean photoluminescent decay time τ of the thin-film and taking the ratio to the decay time of a (powdered phosphor) reference of the same material with a known quantum yield $\eta_{QY,ref}$ and known decay time τ_{ref} (see Supplementary Information for full derivation):

$$\eta_{QY} = \frac{\tau}{\tau_{ref}}\eta_{QY,ref}. \quad (3)$$

Since η_{WG} is not a parameter that depends on our material, but rather on the chosen waveguide, we leave it out of consideration and assume it to be unity.

η_{SA} cannot be measured *per se*, but whether self-absorption occurs can be derived by checking if there is any overlap between the absorption and the luminescent emission of the material. Tm^{2+}-doped halides are already known to have no overlap between their absorption and emission at room temperature [11,12,21].

A high η_{opt} is desirable in an LSC. This high efficiency can, however, not come at a loss of the general window functionality of the LSC. If the LSC absorbs too much light or causes artificial color blindness for a sufficient η_{opt}, it will not make for a good building-integrated photovoltaic equivalent of a window [23]. To quantify how a material would serve as a window, the EN 12646:2011 standard can be taken as guideline.

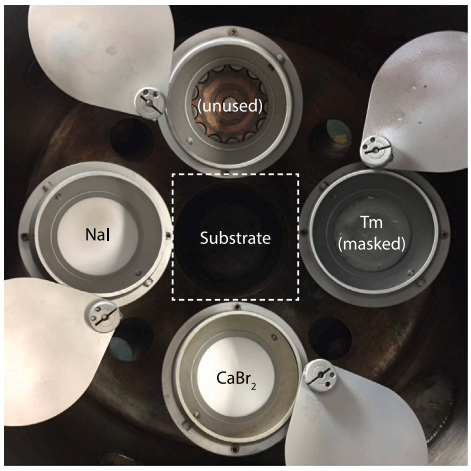

Fig. 1. Example of the layout of the sputtering chamber. The metallic Tm target was used either with a mask on top, reducing the deposition rate for luminescent films, or without to produce highly absorbing films. For absorbing CaI_2:Tm^{2+} films, a pressed powder CaI_2 target took the place of $CaBr_2$, and in the case of luminescent CaI_2:Tm^{2+}, the Tm target was swapped for a pressed powder target made from a mix of 95 % CaI_2 + 5 % TmI_2.

This guideline specifies that a European office requires a correlated color temperature (CCT) between 3000 K and 5300 K and a minimal color rendering index R_a of 80. A high CCT means that the room behind the LSC will look cooler, that is, have a bluer appearance. A low CCT means a warm appearance of the room, that is, a redder, sepia-like appearance. R_a can be calculated from the simulated transmission spectrum of the AM1.5g spectrum through an LSC. This transmission spectrum is expressed as a normalized spectral power distribution [24]. As a reference light source, we use the AM1.5g spectrum. If the CIE 1931 *xyY* color coordinates are calculated from a simulated transmission spectrum (see Ref. [25, Ch. 4]), these coordinates can be translated to the CCT [24,26].

In this article, we determine the optical efficiency η_{opt} of sputter-deposited thin-films of NaI, $CaBr_2$, and CaI_2, doped and more heavily admixed with a concentration gradient of Tm^{2+}. We do so by resolving the parameters constituting η_{opt}, as defined in Eq. (1). First, we determine the luminescent properties of our thin-films. Here the negligible self-absorption η_{SA} of Tm-doped halides is shown. Second, we determine the index of refraction $n(\lambda)$ from these luminescent films using transmission measurements to calculate reflection R and trapping efficiency η_{trap}. Third, we determine the relation between the quantum yield η_{QY} and Tm concentration c_{Tm} by comparing the thin-films to a reference powdered sample. Fourth, we determine the molar absorption coefficient $\varepsilon(\lambda)$, which will provide the absorption efficiency η_{abs}, using transmission measurements of films with high Tm concentrations. Here $\varepsilon(\lambda)$ is checked against the previously measured excitation. Finally, the results of all these measurements are gathered to make predictions on how efficient a thin-film LSC based on the presented materials could be. These simulations are complimented with values for the color rendering index and correlated color temperature.

2. Methods

2.1. Library synthesis

The thulium-doped and more heavily admixed gradient thin-films (hereafter referred to as 'libraries') were combinatorially sputtered in an AJA Orion 8 magnetron sputtering system with a base pressure of 1×10^{-9} bar. A 5-cm-diameter Tm-metal target (4N, Demaco) together with a pressed powder target (pressed at 36 MPa for 5 min), 5 cm in diameter, made from either NaI (4N, Alfa Aesar), $CaBr_2$ (2N5), Alfa

Aesar), or CaI_2 (4N, Alfa Aesar), or a mix of 95 % CaI_2 + 5 % TmI_2 (3N, Sigma Aldrich) were simultaneously RF sputtered at room temperature in a 4×10^{-2} mbar Ar atmosphere (6N, 32 standard cubic centimeters per minute flow rate) onto 5 cm × 5 cm × 0.1 cm borosilicate substrates (PGO). An example of the layout of the sputtering chamber is shown in Fig. 1. Prior to deposition, the substrates were cleaned for 15 min in an ultrasonic bath with a solution of soapy water, after which the substrates were rinsed with acetone and ethanol, followed by a 15 min ultrasonic bath of DI-water. The substrates were dried with a stream of N_2 and left to fully dry in an oven at 200 °C for more than 1 h. The substrate and substrate carrier were heated to 100 °C in the sputtering chamber to prevent moisture contamination. No heating was applied during deposition.

The chimney of the Tm target was masked with a pattern of concentric holes, blocking part of the surface of the chimney and thereby reducing the amount of deposited Tm. The sputter parameters used for the synthesis of all libraries can be found in Table 1.

After deposition, the libraries were removed in a vacuum-tight enclosing and immediately transported to a nitrogen-filled glovebox for storage and further measurements. All powdered samples were fabricated and characterized as described in Ref. [21].

2.2. Luminescence

Fig. 2(a) shows the setup used to record emission spectra. These spectra were recorded by exciting the library locally, using a focused 470 nm LED light source (M470L4, Thorlabs). Excitation light passed through a beam splitter, after which the light was focused on the thin-film. Luminescence was collimated using the same focusing lens. The collimated light was then reflected by the beamsplitter into a 1000 nm long-pass filter (Newport Stabilife 10CGA-1000), which was placed in front of an optical fiber connected to an Ocean Optics NIRQuest512. The *xy*-mapping of local emissions was achieved by placing the library on top of two stacked linear translation stages (LTS150/M, Thorlabs). Emission spectra were recorded using 1 × 4 s integration time over 16 × 16 different positions, with a step size of 3.06 mm between each measurement. Prior to the measurement, the background signal was subtracted by conducting an identical measurement with the LED switched off. All emission measurements were done at room temperature (RT) in a dark nitrogen-filled glovebox.

Excitation spectra were collected at RT using a Horiba QuantaMaster QM-8075-11 spectrofluorometer with two single monochromators and an LN_2-cooled QM-NIR-IGA solid state NIR detector. Luminescence entering the NIR detector was filtered using a 1000 nm long-pass filter (Newport Stabilife 10CGA-1000). The thin-film libraries were placed in a custom sample holder for hygroscopic thin-films, with the film behind a large UV-fused silica window. The sample holder remained filled with N_2 after extraction from the glovebox. Excitation measurements for all libraries were done in three steps: 1. Excitation from 250 nm to 600 nm with a 300 nm long pass excitation filter; 2. Excitation from 350 nm to 800 nm with a 405 nm long pass excitation filter; 3. The same excitation spectra, but with a 800 nm long pass excitation filter to correct for stray light. Emission was recorded at 1137 nm (NaI:Tm^{2+}), or 1140 nm ($CaBr_2$:Tm^{2+}, CaI_2:Tm^{2+}).

2.3. Tm concentration

The local concentration of Tm was determined using electron-dispersive X-ray spectroscopy (EDX) on a JEOL IT-100, operated at 10 keV (films with high Tm content) or 20 keV (films with low Tm content) with probing current at 70 %, under ultra-high vacuum conditions. Quantitative elemental analysis was accomplished by coating the libraries with a 30 nm thick Pd layer after all other analysis steps had been completed. Elemental compositions were quantified at 3000× magnification (31 μm × 23 μm measurement area).

2.4. Transmission

Fig. 2(b) shows the setup used to record transmission spectra. All transmission spectra were measured by placing the libraries between a 2.5 mm diameter collimated (using a Thorlabs RC02SMA-F01) deuterium-halogen (D_2/H) light beam (AvaLight-DH-S, Avantes) and the entrance port of a 5.08 cm diameter integrating sphere (IS200-4, Thorlabs). An Ocean Optics QE65Pro spectrometer (200 μm slit width) and an Ocean Optics NIRQuest512 spectrometer were connected to the off-axis detector port. The libraries were moved through the collimated beam while resting on an anodized Al sample holder, on top of two stacked linear translation stages (LTS150/M, Thorlabs). Transmission spectra were recorded across the libraries at 10 × 10 positions with a step size of 4.2 mm and an integration time of 4 × 500 ms. Dark spectra were recorded by blocking the entrance of the integrating sphere with the edges of the sample holder. Lamp spectra were recorded by directly exposing the integrating sphere to the collimated light. The presented transmission spectra were corrected using these two reference measurements, performed with identical settings. All transmission measurements were carried out at RT in a dark nitrogen-filled glovebox.

2.5. Photoluminescent decay

Decay traces were measured using the same type of setup as described for recording the local emission, shown in Fig. 2(c). In the case of decay traces, the library was excited at 430 nm using a pulsed Ekspla NT230 OPO laser, operating at 33 Hz (3–5 ns FWHM pulse width). These measurements were done at RT outside of the glovebox. To this aim, the libraries were placed in the same sample holder used for the excitation measurements. Luminescence passed through a 1000 nm long-pass filter (Newport Stabilife 10CGA-1000) into an optical fiber which was coupled into an Acton Spect-Pro2300 monochromator coupled to a Hamamatsu H1033A-75 NIR-PMT. The PMT was linked via a pulse-discriminator to a CAEN DT5724F Digitizer. This setup was used for time-correlated single photon counting. Because of the large amount of data coming from the digitizer (40 ms of data, i.e., ∼ 40 million channels of raw 12 bits data, which would mean that 1 sample can be processed per second over USB 2.0, whereas 33 samples are produced each second), the internal decimation option of the digitizer was used for online averaging. This decimation from online averaging over 7^2 = 49 traces led to the 33 Hz laser being the limiting factor in data output. In total, each data point is an average of 2000 decay traces.

3. Results and discussion

3.1. Local luminescence

Figs. 3(a), 3(d) and 3(g) show the local Tm concentration for all emitting films. EDX measurements give the local chemical composition of the gradient thin-films at 36 positions. These measurements are accurately fit (RMSE < 0.31 at.%) and interpolated with the surface-source evaporation equation [27,28]. From these fits, it follows that the Tm concentration varies from 0.29 at.% to 3.0 at.% in the NaI:Tm^{2+} film, from 0.13 at.% to 4.8 at.% in the $CaBr_2$:Tm^{2+} film, and 0.46 at.% to 4.6 at.% in the CaI_2:Tm^{2+} film.

The emission of the thin-films was measured as deposited, without any further treatment. All areas of the thin-films emit 4f-4f line emission at approximately 1140 nm after excitation at 470 nm, as seen in Figs. 3(b), 3(e) and 3(h). Scanning over the entire thin-film concentration gradient shows that the emission at 1140 nm occurs independent of concentration. While a difference in emission intensity is visible that could be correlated with the Tm concentration, this does not have to imply more efficient luminescence. The observed emission intensity is dependent on the film's local morphology (which is responsible for light scattering and thereby light collection efficiency), quantum yield, and amount of absorption. Therefore, it is necessary to individually measure

Table 1
Sputter parameters used in the synthesis of the various libraries. Two libraries are produced for each material type: One for the measurement of luminescent properties, typically with lower Tm powers applied, resulting in a film doped with 0.1–4.8 at.% Tm, indicated with (L). The other with higher Tm powers applied, yielding 4.7–54 at.% Tm, for determination of the absorption coefficient, indicated with (A).

Library	Power on Tm (W)	Reducing mask installed?	Power on host (W)	Duration (h)	Orientation host/Tm (see Fig. 1)
$CaBr_2:Tm^{2+}$ (L)	30	Yes	80	2	Bottom/Right
$CaBr_2:Tm^{2+}$ (A)	30	No	80	1	Bottom/Right
$CaI_2:Tm^{2+}$ (L)	50[a]	[a]	120	8	Bottom/Right
$CaI_2:Tm^{2+}$ (A)	13	No	120	4	Bottom/Right
$NaI:Tm^{2+}$ (L)	20	Yes	35	2	Left/Right
$NaI:Tm^{2+}$ (A)	30	No	35	1	Left/Right

[a]A mixed-powder 95% CaI_2 + 5% TmI_2 target was used instead of the Tm metal target.

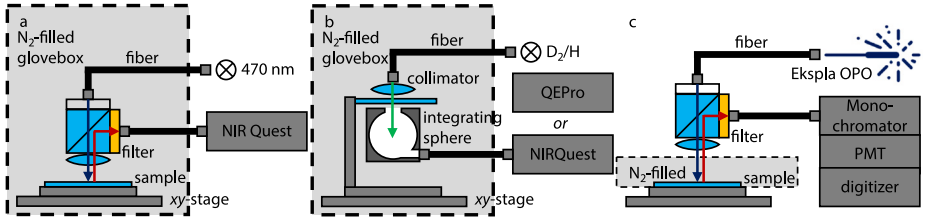

Fig. 2. Setups used to measure local luminescent properties. a: Local emission setup in glovebox. b: Local transmission setup in glovebox. c: Local decay setup with custom N2-filled sample holder.

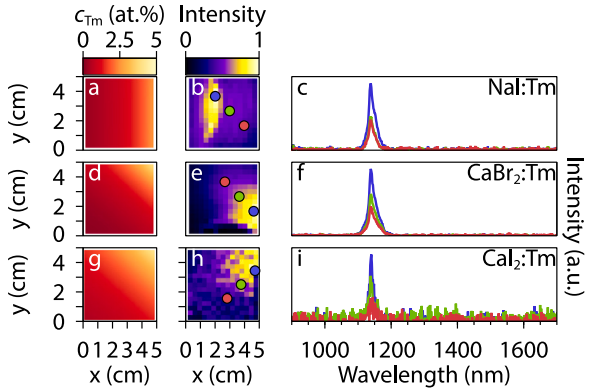

Fig. 3. Local properties of the investigated films. a, d, g: Local Tm concentration c_{Tm}. b, e, h: Emission intensity at 1137 nm for $NaI:Tm^{2+}$, or 1140 nm, for $CaBr_2:Tm^{2+}$ and $CaI_2:Tm^{2+}$ after excitation at 470 nm mapped across the gradient film, normalized to the most intense emission. c, f, i: Emissions of the locations marked in the preceding panel. Panels a, b, c apply to the $NaI:Tm^{2+}$ gradient thin-film; panels d, e, f apply to the $CaBr_2:Tm^{2+}$ gradient thin-film; panels g, h, i apply to the $CaI_2:Tm^{2+}$ gradient thin-film.

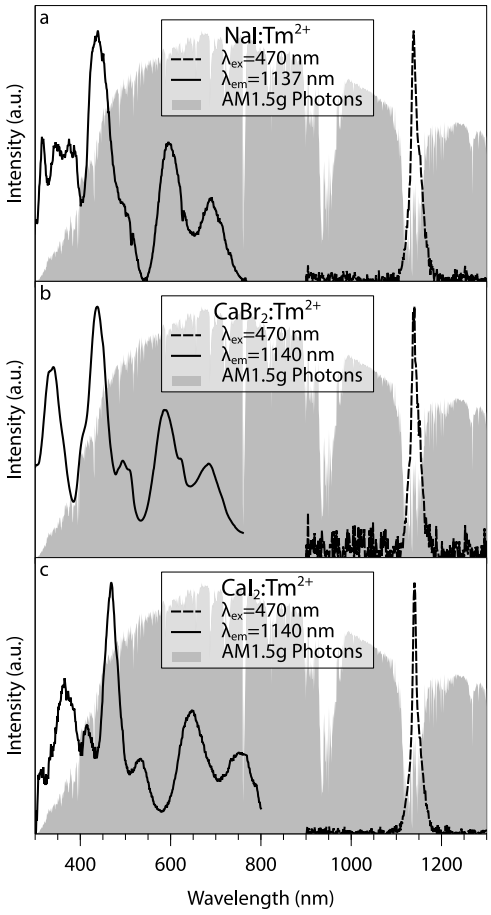

Fig. 4. Excitation and emission spectra for a: $NaI:Tm^{2+}$, b: $CaBr_2:Tm^{2+}$, c: $CaI_2:Tm^{2+}$ thin-films superimposed on the AM1.5g solar spectrum. All spectra clearly display the typical 4f-5d bands in excitation, which leads to the distinct $^2F_{5/2}\rightarrow{}^2F_{7/2}$ 4f-4f emission centered at approx. 1140 nm. For all materials, the 4f-5d excitation bands cover the entire visible spectrum.

the absorption strength and the quantum yield of a Tm center, as will be done in the later sections.

Fig. 4 shows the excitation spectra (solid line) of the $^2F_{5/2}\rightarrow{}^2F_{7/2}$ Tm^{2+} emission (dashed) for (a) $NaI:Tm^{2+}$, (b) $CaBr_2:Tm^{2+}$, and (c) $CaI_2:Tm^{2+}$, with the AM 1.5g solar spectrum in the background. The excitation spectrum exhibits several $4f^{13} \rightarrow 4f^{12}5d^1$ broad-band transitions in the range of 200-800 nm. The mechanism for splitting of Tm^{2+} 4f-5d transitions and the shift of excitation wavelength in different halides is described in detail in Ref. [12]. What can be concluded from Fig. 4 is that Tm^{2+} shows no overlap between 5d-4f excitation and f-f emission and is unlikely to show self-absorption of the emission at 1140 nm. It is still possible for self-absorption through the $^2F_{5/2}\rightarrow{}^2F_{7/2}$ transition itself to occur (f-f absorption). f-f absorption is, however, very weak, typically over 100 times weaker than the f-d absorption [12].

3.2. Thickness and index of refraction

As written in the introduction, we are seeking to individually resolve the factors required to calculate the optical efficiency of an LSC (Eq. (1)). In Eq. (1), we first encounter the amount of reflection from the top surface R. R is a function of the complex index of refraction

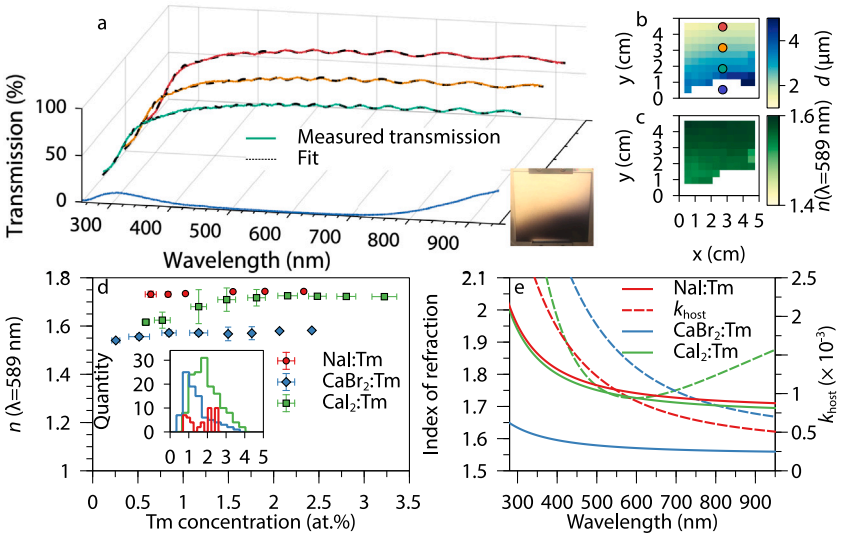

Fig. 5. Properties extracted from fitting the local transmission of the thin-films with the Extended-Sellmeier method. a: Transmissions measured at the locations indicated in panel b and accompanying fits. Close to the $CaBr_2$ gun, the transmission suddenly decreases (blue curve), as also visible in the inset. b: Thickness distribution for $CaBr_2$:Tm^{2+} in μ m. The white area marks where adjusted-R^2<0.99 due to sudden high absorption of the thin-film. c: Local index of refraction n of the $CaBr_2$:Tm^{2+} thin-film. d: n for all Tm concentrations on the thin-films, grouped per concentration. The inset shows how the measured locations were distributed in these groups. Groups with less than 3 measured locations are not shown. e: Index of refraction (solid lines) and host extinction (dashed lines) at 1 % Tm concentration.

$\tilde{n}(\lambda) = n(\lambda) + ik(\lambda)$, as is trapping efficiency η_{trap}, later encountered in Eq. (1). Retrieving $\tilde{n}(\lambda)$ will thus give us both R and η_{trap}. We can locally extract $\tilde{n}(\lambda)$ from transmission spectra, by using the Extended-Sellmeier method [9,29]. This method also gives the local thickness of the thin-film.

These fitted (adjusted-R^2>0.99) local transmission measurements, shown for $CaBr_2$:Tm^{2+} in Fig. 5(a), agree very well with what we expected. All films show a gradient in thickness that is proportional to the distance from the sputter gun that carried the host. From Fig. 5(b), we see that the film thickness of $CaBr_2$:Tm^{2+} varies from 1.4 μm to 4.5 μm, while the refractive index (Fig. 5(c)) stays relatively constant, between 1.55 and 1.58 at λ =589 nm. The refractive indices can be directly related to the concentration, using the concentration data from Fig. 3(d). Fig. 5(d) shows that n rises slightly as the Tm concentration increases. The fitted n agrees well with values for other bromide-type materials, such as KBr and RbBr, with refractive indices of 1.560 and 1.553 at λ =589 nm, respectively [30]. As can be seen from Fig. 5(a), the many 5d-bands of Tm cannot be resolved from transmission data. Therefore, only the extinction coefficient of the host k_{Host} is resolved.

At very low Tm concentrations (low y in Fig. 5(b)), the fit quality reduces due to a sudden decrease in transmission, caused by an intense absorption, as can be seen from the dark area on the photograph in the inset of Fig. 5(a). This absorption can be seen as the lowest, blue line in Fig. 5(a). We tentatively attribute this sudden absorption to a non-stoichiometric number of anions to cations, as is often observed when sputtering from ceramic sources in a non-reactive environment [31, p. 479], which leads to the formation of highly absorbing color centers. The locations that show this type of absorption are not included in our subsequent analysis.

For CaI_2 and NaI, the wavelength-dependent index of refraction is also shown in Fig. 5(e). The value of n at 589 nm, shown in Fig. 5(d), is around 1.75 for NaI:Tm^{2+} and around 1.73 for CaI_2:Tm^{2+}. These values agree well with the 1.774 reported for NaI in literature [30]. For all materials, k_{Host} is shown in Fig. 5(e). This host absorption is quite low and should therefore not be taken as a very precise fitting.

3.3. Photoluminescent quantum yield

The second parameter required to simulate LSC performance, is the concentration-dependent quantum yield $\eta_{QY}(c_{Tm})$. Tm^{2+}, when embedded in halides, can display many types of photoluminescent decay processes [21]. In this article, we are solely interested in emission from the $^2F_{5/2}\rightarrow{}^2F_{7/2}$ transition (emission at 1140 nm).

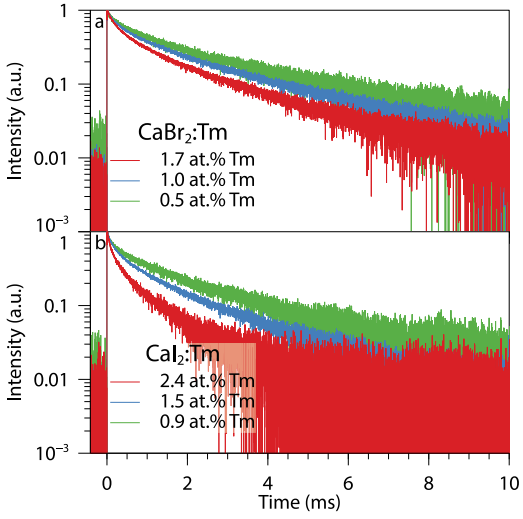

Fig. 6. Decays of a: $CaBr_2$:Tm^{2+}, b: CaI_2:Tm^{2+}, after excitation at 430 nm at various Tm concentrations.

To determine $\eta_{QY}(c_{Tm})$, we have to know which energetic path Tm^{2+} takes to get from its excited state to the ground state. which can be done by monitoring the photoluminescent decay. In Fig. 6, the photoluminescence decay curves are shown for the $^2F_{5/2}\rightarrow{}^2F_{7/2}$ transition for (a) $CaBr_2$:Tm^{2+}, and (b) CaI_2:Tm^{2+}, respectively. These transitions have a decay time ranging across several milliseconds, typical for the parity-forbidden f-f transition. With higher Tm-doping, the transition becomes faster, which is most likely related to concentration quenching [32, Ch. 5].

Illumination with 430 nm light first leads to a $4f^{13} \rightarrow 4f^{12}d^1$ excitation, which can relax back to either the $^2F_{5/2}$ excited f-state, or the $^2F_{7/2}$ groundstate. Since no rise-time of the $^2F_{5/2}\rightarrow{}^2F_{7/2}$ emission is observed in $CaBr_2$:Tm^{2+} and CaI2:Tm, we do not expect there to be sufficient time for energy transfer from the excited 5d-state to neighboring ions. Thus, the non-radiative decay from the 5d-state is independent of Tm

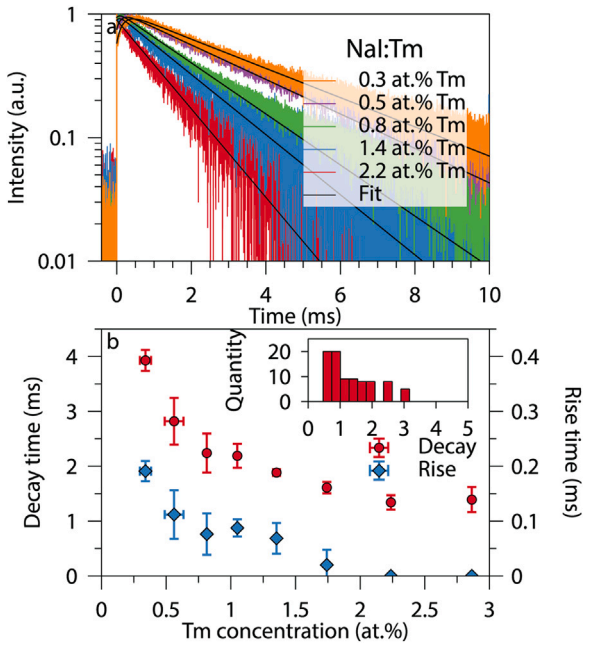

Fig. 7. Photoluminescent decay of NaI:Tm^{2+} after excitation at 430 nm. a: Decay at several Tm concentrations. Black lines through the curves are fits according to Eq. (4). b: Distribution of the results of the fitting of the decay and rise-time (red dots and blue diamonds, respectively associated with the left and right vertical axes) for all Tm concentrations measured. The inset shows how the different measurements were grouped according to Tm concentration.

concentration. The quantum yield of our entire system is therefore defined as:

$$\eta_{QY}(c_{Tm}) = \eta_{5d\rightarrow {}^2F_{5/2}}\eta_{QY,{}^2F_{5/2}\rightarrow {}^2F_{7/2}}(c_{Tm}),$$

with $\eta_{5d\rightarrow {}^2F_{5/2}}$ the concentration-independent quantum yield at which excited 5d-states decay back to the $^2F_{5/2}$ excited state.

If the system reaches the $^2F_{5/2}$ state, non-radiative return to the groundstate can either happen independently of Tm concentration through multiphonon relaxation, in accordance with the modified energy gap law [33], or through the aforementioned concentration quenching. The $^2F_{5/2}\rightarrow {}^2F_{7/2}$ transition is therefore described by a simple two-level system, with the non-radiative decay rate $\Gamma_{nr}(c_{Tm})$ and radiative decay rate Γ_{rad}. This gives for the quantum yield of the 4f-4f emission:

$$\eta_{QY,{}^2F_{5/2}\rightarrow {}^2F_{7/2}}(c_{Tm}) = \frac{\Gamma_{rad}}{\Gamma_{rad} + \Gamma_{nr}(c_{Tm})}.$$

In NaI:Tm^{2+}, the photoluminescent decay becomes more complicated. As seen in Fig. 7(a), when monitoring the intensity of the $^2F_{5/2}\rightarrow {}^2F_{7/2}$ emission over time, a rise-time can be observed. Contrary to what is observed for $CaBr_2$:Tm^{2+} and CaI_2:Tm^{2+}, the system appears to remain in the excited 5d-state sufficiently long for energy migration to happen. This rise-time can be attributed to a feeding from the higher lying 5d-states to the excited $^2F_{5/2}$ level. The rise-time $\tau_{rise}(c_{Tm})$ and the luminescent decay of the $^2F_{5/2}$level can be modeled as simple exponential decays, with A and B fitting constants:

$$I(t) = A\exp\left(-\frac{t}{\tau(c_{Tm})}\right) + B\exp\left(-\frac{t}{\tau_{rise}(c_{Tm})}\right) \quad (4)$$

As seen in Fig. 7(b), both the decay times and the rise-times decrease with an increase in Tm concentration. In this article, we will not go into the details of this complicated decay process. However, to still give an upper bound for $\eta_{QY}(c_{Tm})$, the fitted decay times for NaI can be treated in the same way as those for $CaBr_2$:Tm^{2+} and CaI_2:Tm^{2+}. We choose to neglect the rise-times and the impact of the system remaining longer

Table 2
Measured mean decay times and quantum yields for powdered samples with Tm concentration $c_{Tm,ref.}$. $\tau_{ref.}$ is the mean decay time of the reference powder measured at excitation wavelength $\lambda_{ex,decay}$. $\eta_{QY,ref.}$ is the measured quantum yield at excitation wavelength $\lambda_{ex,QY}$.

Powdered sample	$\lambda_{ex,decay}$ (nm)	$\tau_{ref.}$ (ms)	$\lambda_{ex,QY}$ (nm)	$\eta_{QY,ref.}$ (%)	c_{ref} (at.%)
NaI:Tm^{2+}	420	3.0	715	33.2	0.86
$CaBr_2$:Tm^{2+}	420	4.1	645	22.4	1.2
CaI_2:Tm^{2+}	475	3.7	760	28.1	0.8

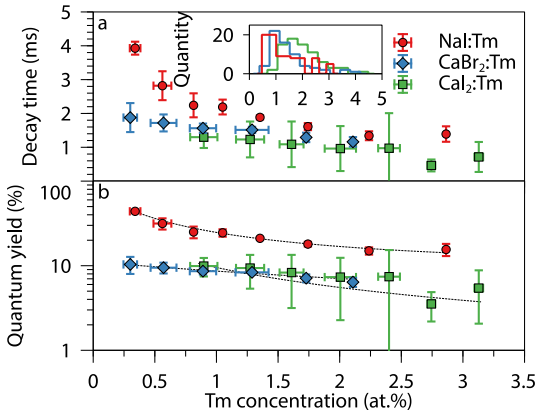

Fig. 8. Luminescent lifetimes of all films studied. a: Mean decay time per concentration after excitation at 430 nm. The inset shows the distribution of Tm concentrations. Only concentrations with more than 2 measured points are shown in panels a and b. b: Estimated quantum yield, calculated using reference powder, following Eq. (3). Note that these quantum yields are an upper bound for the true quantum yield. This upper bound especially applies to NaI:Tm^{2+}, which displays rise-times from higher lying d-states. The dashed line is a best fit, following a logistic curve.

in the excited 5d-state, and therefore assume there is no significant concentration quenching by energy migration in the 5d excited state.

The (assumed) concentration-independence of the non-radiative relaxation from the 5d-levels to the 4f-levels makes it possible to give an estimate of $\eta_{QY}(c_{Tm})$ based on $\tau(c_{Tm})$, combined with a reference measurement of $\eta_{QY,ref.}$ and the mean decay time $\tau_{ref.}$ from a powder made of the same material, in accordance with Eq. (3). These reference measurements have been made for NaI:Tm^{2+}, $CaBr_2$:Tm^{2+}, CaI_2:Tm^{2+} powders. $\tau_{ref.}$ and, for $CaBr_2$:Tm^{2+} and CaI_2:Tm^{2+}, $\tau(c_{Tm})$ are calculated as a mean decay time:

$$\tau = \frac{\int_0^\infty tI(t)\,dt}{\int_0^\infty I(t)\,dt}, \quad (5)$$

with $I(t)$ the luminescence intensity over time t.

For NaI:Tm^{2+}, $\tau(c_{Tm})$ is the decay time presented in Fig. 7(b). $\tau_{ref.}$ and $\eta_{QY,ref.}$ for all powdered samples are displayed in Table 2.

Using Eq. (5) and by overlaying the decay data with our previously measured data on the local c_{Tm} (Figs. 3(a), 3(d) and 3(g)), we can calculate $\tau(c_{Tm})$ for our $CaBr_2$:Tm^{2+} and CaI_2:Tm^{2+} films (see Fig. 8(a)). As shown in Fig. 8(b), $\eta_{QY}(c_{Tm})$ is calculated from $\tau(c_{Tm})$ and the data from the reference powders (Table 2) using Eq. (3). $\eta_{QY}(c_{Tm})$ decreases from 10 % at 0.3 at.% Tm to 6.4 % at 2.1 at.% Tm in CaBr2:Tm, and from 10 % at 0.9 at.% Tm to 5.4 % at 3.1 at.% Tm in CaI2:Tm. For NaI:Tm^{2+}, $\eta_{QY}(c_{Tm})$ decreases from 44 % at 0.3 at.% Tm, to 15 % at 2.9 at.% Tm. Because of the rise-time, the calculated quantum yields from Fig. 8(b) are an upper bound for $\eta_{QY}(c_{Tm})$ of NaI:Tm^{2+}.

What should be remarked here is that for the thin-films, the decay times are consistently lower than for the powders at equal Tm concentration. At 0.8 at.%, the $^2F_{5/2}\rightarrow {}^2F_{7/2}$ transition of NaI:Tm^{2+} has a decay time of about 2.2 ms, compared to 3.0 ms in the powder. For the dihalides, at approximately equal dopant concentrations the decays are 1.5 ms and 1.3 ms, respectively for $CaBr_2$:Tm^{2+} and CaI_2:Tm^{2+} in

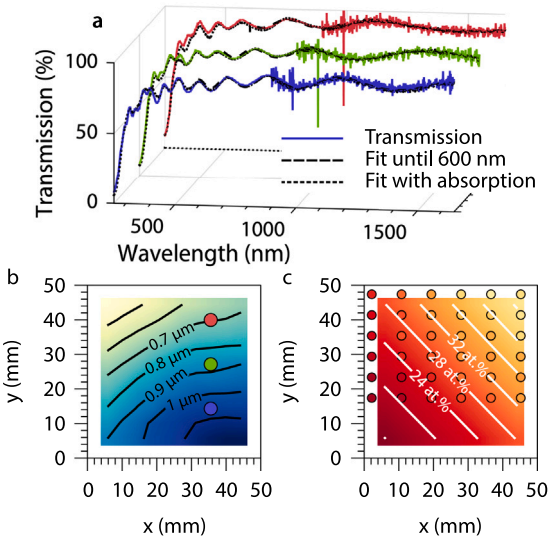

Fig. 9. Properties of the absorbing $CaBr_2$:Tm^{2+} film. a: Local transmission spectra collected at locations marked in panel b. Solid lines show the measured transmission. Dashed lines show a fit to the absorption in wavelength-domain where the library does not strongly absorb, 600 nm until 1600 nm. Dotted lines show the fit that does include the absorption. b: Thickness of the library, as determined by fitting the transmission from 600 nm until 1600 nm. c: Tm concentration across the library determined by fitting the surface-source evaporation equation through local EDX measurements. Dots show the local EDX measurements. The color of those dots uses the same colormap as the contour plot of the fitted concentration. The color of the dot therefore shows the measured Tm concentration. The fit is cropped to coincide with the transmission measurement.

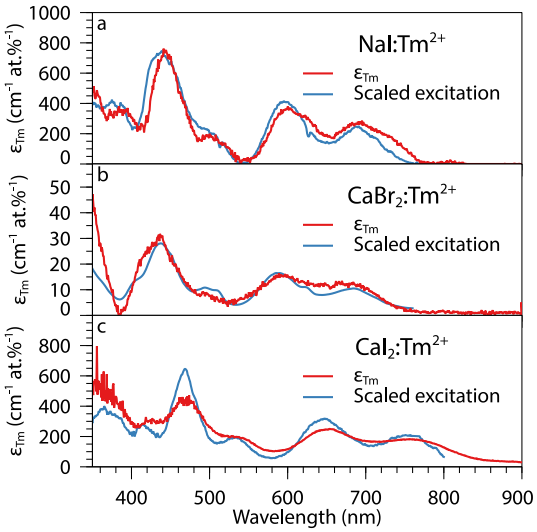

Fig. 10. Fitted absorption strength (measured on libraries with a high Tm^{2+} concentration) of all halides under consideration compared to their respective excitation spectra (measured on libraries with a low Tm^{2+} concentration), as presented in Fig. 4. a: Absorption for NaI:Tm^{2+}. b: Absorption for $CaBr_2$:Tm^{2+}. c: Absorption for CaI_2:Tm^{2+}.

films, and 4.1 ms and 3.7 ms, respectively in powders. This mismatch between the decay times at equal concentrations can be explained by the higher amount of defects and therefore quenching sites in the thin-films. Even though higher quantities of Tm^{2+} amend the vacancies caused by a shortage of cations, the films are not expected to be perfectly stoichiometric.

3.4. Absorption of thulium

The third requirement to simulate LSC performance is the concentration-dependent absorption of our Tm-doped halides. The concentration of Tm in the luminescent libraries presented before is too low to measure absorption. Therefore, we deposited films with the same hosts, under the same synthesis conditions, but with a less dense mask on the Tm target to warrant a higher Tm deposition rate. Similar to the films with a lower Tm concentration, rasterized transmission measurements were carried out across these thin-films. The higher Tm deposition rate yields films displaying very pronounced Tm absorption. For instance, in $CaBr_2$:Tm^{2+}, seen in Fig. 9(a), we can observe that the normally gradual interference pattern (seen in Fig. 5(a) for the $CaBr_2$:Tm^{2+} film with low absorption) has the characteristic Tm^{2+} 4f-5d transition spectrum (as seen in Fig. 4(b)) superimposed. The sharp drop-off of the transmission below 320 nm is due to the substrate, made from borosilicate glass. The high absorption of Tm makes it impossible to use the Extended-Sellmeier method reliably for wavelengths below 600 nm. Therefore, the thickness and index of refraction of these films are determined by expanding the measured transmissions to the near-infrared. Fitting is now done in the wavelength domain from 600 nm to 1600 nm, where the libraries do not absorb. Fig. 9(a) shows that this still leads to fits of high quality (average RMSE of 2.5 %). The dashed curve from the fitting can hardly be discerned from the dotted measured transition. These fits yield the local thickness d, as seen for the absorbing $CaBr_2$:Tm^{2+} in Fig. 9(b).

Following the same EDX protocol as before, the local Tm concentration is determined (RMSE < 1.8 %). In these three films with a higher Tm concentration, the Tm concentration varies from 4.7 at.% to 7.4 at.% in the NaI:Tm^{2+} film, from 16 at.% to 44 at.% in the $CaBr_2$:Tm^{2+} film (see Fig. 9(c)), and 45 at.% to 54 at.% in the CaI_2:Tm^{2+} film. In the Supplementary Information, representative measurements for all three libraries can be found.

With d, n, k_{Host} and c_{Tm} now determined for the chosen hosts, we can utilize the minimization protocol described in the Supplementary Information and obtain the absorption coefficient $\varepsilon_{Tm}(\lambda)$. In Fig. 10, the results of this minimization are displayed for all hosts under consideration. As expected, ε_{Tm} closely follows the excitation spectrum. In a study on crystalline Tm-doped perovskites, high f-d absorption strengths of hundreds of cm^{-1} at.%$^{-1}$ were found [18]. In our current study, we find similarly large values, but then measured through thin-film transmission using a wide range of concentrations. In the visible spectrum, from 400 nm to 750 nm, NaI:Tm^{2+} has a visible absorption maximum of 752 cm^{-1} at.%$^{-1}$ at 444 nm, $CaBr_2$:Tm^{2+} 31 cm^{-1} at.%$^{-1}$ at 437 nm, and CaI_2:Tm^{2+} 473 cm^{-1} at.%$^{-1}$ at 472 nm. The cause of the lower absorption of $CaBr_2$:Tm^{2+} compared to the other halides is beyond the scope of this study.

3.5. Prognosis for a luminescent solar concentrator

We now have all parameters required to simulate the optical efficiency of a thin-film LSC without self-absorption, for any desired Tm concentration and thickness. To simulate this LSC, we can follow a protocol similar to the one presented in Ref. [9]. Using the transfer matrix method, implemented by using the free open-source `tmm` module [34], the reflection $R(\lambda, c_{Tm}, d)$ and transmission $T(\lambda, c_{Tm}, d)$ of an LSC comprising a film of thickness d coated on 5 mm thick BOROFLOAT®33 glass is calculated. BOROFLOAT is chosen as substrate, since it has negligible absorption at the emission wavelength of Tm. For the thin-film, the complex index of refraction

$$\tilde{n}(\lambda, c_{Tm}) = n(\lambda, c_{Tm}) + ik(\lambda) \times c_{Tm}$$

is used, with $n(\lambda, c_{Tm})$ as presented in Figs. 5(b) and 5(c), and $k(\lambda)$ as presented in Fig. 10, calculated with Eq. (2). These numbers are converted to fractions of the AM1.5g solar spectrum $S_{AM1.5g}(\lambda)$, with

$$T_{total}(d, c_{Tm}) = \frac{\int_0^\infty S_{AM1.5g}(\lambda) T(\lambda, d, c_{Tm})\, d\lambda}{\int_0^\infty S_{AM1.5g}(\lambda)\, d\lambda}.$$

Table 3
Results of simulating thin-film LSCs coated on 1 mm thick BOROFLOAT®33 glass with a thickness constraint of 10 μm.

Material	d (μm)	c_{Tm} (at.%)	T (%)	η_{opt} (%)	CCT (K)	R_a
NaI:Tm^{2+}	10	1.6	80	0.35	5301	96
$CaBr_2$:Tm^{2+}	10	2.1	90	0.03	5820	99
CaI_2:Tm^{2+}	10	1.8	62	0.30	4586	90

The total amount of reflection $R_{total}(d, c_{Tm})$ is calculated analogously.

Absorption is calculated as

$$A_{total}(d, c_{Tm}) = 1 - T_{total}(d, c_{Tm}) - R_{total}(d, c_{Tm}).$$

All absorbed light is converted with the fitted quantum yield $\eta_{QY}(c_{Tm})$ from Fig. 8(b). This converted light is then concentrated to the perimeter of the LSC. Since our films do not exhibit self-absorption, the amount of concentrated light can be calculated by multiplying the amount of converted light $I_{converted}(d, c_{Tm})$ with the trapping efficiency [35]

$$\eta_{trap}(\lambda, c_{Tm}) = \frac{\sqrt{n(\lambda, c_{Tm})^2 - 1}}{n(\lambda, c_{Tm})},$$

yielding the optical efficiency

$$\eta_{opt}(d, c_{Tm}) = A_{total}(d, c_{Tm})\eta_{QY}(d, c_{Tm})\eta_{trap}(\lambda = 1140\ \text{nm}, c_{Tm}).$$

Since our films do not exhibit self-absorption, the calculated $\eta_{opt}(d, c_{Tm})$ is the same for every planar size of the LSC, assuming no further waveguide losses.

If the Tm concentration is sufficiently low that no concentration quenching is occurs, the only limitations on η_{opt} of the halide systems would be the total absorption of the thin-film, and the loss channels present in the single ion $\eta_{QY}(c_{Tm} \to 0)$. In the presented systems, at an absorption of 80 % of the visible spectrum, that would imply a maximal $\frac{\eta_{opt}}{\eta_{QY}(c_{Tm}\to 0)} = A_{total}\eta_{trap}$ of 3.5 % for NaI:Tm^{2+}, 3.9 % for $CaBr_2$:Tm^{2+}, and 4.2 % for CaI_2:Tm^{2+}. For films with a constraint on thickness however, a balance must be struck between the absorption and quantum yield.

For our simulation, we have chosen three situations: a thin-film LSC with

1. A thickness of at most 10 μm.
2. An additional constraint of at least 80 % transmission of the visible spectrum, expressed in photons
$$T_{vis}(d, c_{Tm}) = \frac{\int_{\lambda=380\ nm}^{780\ nm} S_{AM1.5g}(\lambda) T(\lambda, d, c_{Tm})\, d\lambda}{\int_{\lambda=380\ nm}^{780\ nm} S_{AM1.5g}(\lambda)\, d\lambda} = 0.8.$$
3. The same conditions as the previous simulations, but with the decays scaled such that all films perform equal to their powdered counterparts, i.e., instead of using Eq. (3), we state that
$$\eta_{QY,film}(c_{Tm}) = \frac{\tau_{film}(c_{Tm})}{\tau_{film}(c_{Tm,ref})}\eta_{QY,powder}(c_{Tm,ref}).$$

With regards to the situations, a constraint for a thickness of 10 μm is chosen to remain within what is achievable for the used sputter system. As films become thicker, the amount of stress in the film increases, therefore so does the chance of delamination. Therefore, a thin-film is preferred over a thicker film.

Table 3 shows these results for the final η_{opt}, CCT and R_a for the first situation, where the film thickness is limited to 10 μm. From Table 3, we can see that a 10 μm halide thin-film, as sputtered, can maximally achieve $\eta_{opt} = 0.35\%$ for a NaI:Tm^{2+} thin-film, with a doping of 1.6 at.% Tm, while retaining an excellent CCT and R_a. Here we do have to remark that NaI:Tm^{2+} has a $\eta_{QY}(c_{Tm})$ that is estimated to be on the high end, by neglecting the rise-time phenomena.

In Fig. 11, the fates of all photons incident on the simulated LSCs are shown. In the best performing NaI:Tm^{2+} (Fig. 11(a)), most light is lost to reflection (9.9 % of all sunlight, including ultraviolet and infrared) and transmission (87.9 %). At this thickness, the absorption could be increased, but that would come at a loss of quantum yield, which would not be compensated by the increased absorption. Due to the non-unity quantum yield, 80.5 % of absorbed light (1.8 % of all light) is lost by quenching. After this conversion step, still 3.7 % of the absorbed light (0.08 % of all light) escapes. Eventually, 15.8 % of the absorbed light will be concentrated to the edges of the window. Increasing the quantum yield is therefore key for this material.

Table 4
Simulation outcome with the additional constraint of 80% transmission applied. The last two entries are provided for comparison. These entries show simulated high-performance LSCs consisting of a 100 cm × 100 cm × 0.5 cm PMMA waveguide, with non-scattering luminescent particles dispersed within.

Material	d (μm)	c_{Tm} (at.%)	T (%)	η_{opt} (%)	CCT (K)	R_a
NaI:Tm^{2+}	10	1.6	80	0.35	5301	96
$CaBr_2$:Tm^{2+}	10	2.1	90	0.03	5820	99
CaI_2:Tm^{2+}	7	0.9	80	0.18	5342	96
Red305 [3,36]	5.0×10^3	–	80	3.5	5077	66
$CuInS_2$/ZnS [3,37]	5.0×10^3	–	80	2.8	4868	98

Table 5
Results of simulating 10 μm thick thin-film LSCs coated on BOROFLOAT®33 glass, 1 mm in thickness. The quantum yields of the Tm^{2+} are scaled so that at equal concentrations, films and powders perform the same.

Material	d (μm)	c_{Tm} (at.%)	T (%)	η_{opt} (%)	CCT (K)	R_a
NaI:Tm^{2+}	10	1.6	80	0.71	5301	96
$CaBr_2$:Tm^{2+}	10	2.1	90	0.07	5820	99
CaI_2:Tm^{2+}	10	1.8	62	0.39	4586	90
CaI_2:Tm^{2+}	7	0.9	80	0.24	5342	96

From Fig. 11, the differences between the three simulated films and their performances become clear. While CaI_2:Tm^{2+} (Fig. 11(c)) has the lowest $\eta_{QY}(c_{Tm})$ of all three sputtered halides, the high absorption makes it possible to achieve a η_{opt} that is higher than for $CaBr_2$:Tm^{2+} (Fig. 11(b)), at the same thickness. This high absorption does come with a loss of R_a and CCT. Whereas the other thin-film LSCs retain CCTs of 5000–6000 K and almost perfect R_a, in the case CaI_2:Tm^{2+}, the high absorption of the blue wavelengths leads to warmer coloring of 4586 K, and an R_a of 90.

Table 4 shows what happens when further constraining the film to transmit 80 % of the visible spectrum. Such constraints on transmission better emulate what would be applicable as a BIPV window. The additional constraint causes CaI_2:Tm^{2+} to drop in efficiency. Due to its high absorption coefficient, a reduction in absorption is only possible when both the film thickness and Tm concentration drop significantly. Even though a lower Tm concentration implies less concentration quenching and therefore a higher quantum yield, this is not enough to offset the decrease in efficiency that CaI_2:Tm^{2+} would gain from having high absorption. The other halides already showed 80 % transmission as optimal for 10 μm, therefore the simulation results for those are identical to the ones presented in Table 3.

Table 4 provides a comparison of the LSCs studied in this article to 100 cm × 100 cm × 0.5 cm PMMA plates with BASF Lumogen F Red 305 (Red305) or $CuInS_2$/ZnS colloidal quantum dots (QDs) dispersed within, held to the same constraint of 80 % transmission. Red305 features unity quantum yield [36], and the $CuInS_2$/ZnS QDs has a quantum yield of 66 % when dispersed in a waveguide [37]. Even though these LSCs show self-absorption, their high quantum yields let them reach much higher efficiencies than the optical efficiencies observed in the halides under study.

Table 5 shows the results of the same types of simulations, but then for the final situation. Here, the quantum yields of the films are scaled so that they perform equal to their powdered counterparts at the same concentration, but retain the concentration quenching

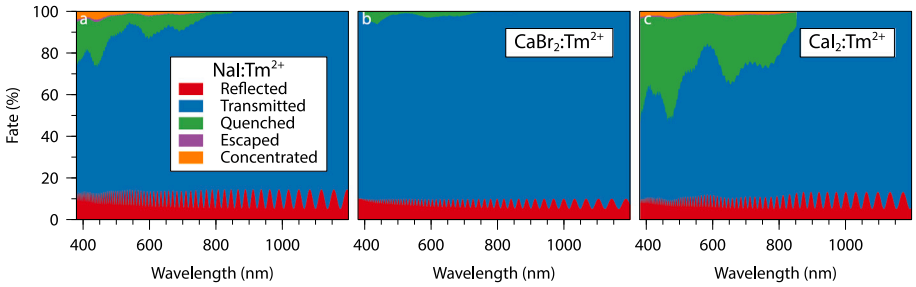

Fig. 11. Fates of all incident photons for the best performing simulated halide thin-film LSCs with a coating thickness of 10 μm and no constraints on the total transmission. a: NaI:Tm^{2+}, b: $CaBr_2$:Tm^{2+}, c: CaI_2:Tm^{2+}.

behavior measured in the thin-films. It can be possible to achieve similar quantum yields as in powders: a film with thickness of 10 μm, has a similar smallest dimension as typically grains of luminescent powder have. The films and the powder therefore can both behave as bulk materials with similar quantum yields. Due to the much increased quantum yield of NaI:Tm^{2+}, its optical efficiency as a 10 μm thick coating doubles, from 0.35 % to 0.71 %. This doubling in efficiency is also seen for $CaBr_2$:Tm^{2+}, but its low absorption causes it to still display the lowest η_{opt}. At these raised quantum yields, the halide thin-films can be seen as good competitors to the Red305 dye, as well as to the $CuInS_2$/ZnS QDs. Even though the efficiencies for the halide LSCs are not as high, their excellent color rendering indices and neutral CCT still make them suitable for integration in the built environment.

4. Conclusion

NaI, $CaBr_2$, and CaI_2 doped with Tm^{2+}, that have previously been suggested as materials for a thin-film LSC, have in this article been investigated on their potential as LSCs. These films prove viable as LSC materials, absorbing the entire visible spectrum and emitting at 1140 nm, without self-absorption. When sputtered from separate targets, with one target containing the host, and another containing the Tm dopant, substoichiometry of the deposited films can be observed, expressed as deep absorption. The large number of defects in the thin-films can explain the lower decay times, and therefore lower quantum yield of the films, when compared to powders made from the same materials. All films under investigation show quenching of luminescence, even at concentrations as low as 0.3 at.% Tm.

NaI:Tm^{2+} and CaI_2:Tm^{2+} show high absorptions of respectively 752 cm^{-1} at.%$^{-1}$, and 473 cm^{-1} at.%$^{-1}$. In the case of NaI:Tm^{2+}, this leads to the highest simulated LSC optical efficiency of 0.35 % (15.8 % concentration of all absorbed light), at 80 % visible light transmission, using the measured data from thin-films. In the absence of defects caused by sputtering, this efficiency can rise to 0.71 % (31.5 % concentration of all absorbed light), compared to a maximally achievable optical efficiency of 3.5 %. A challenge for future research is therefore to resolve the defects present in the films, and thus increase the quantum yield. This could be achieved with post-synthesis treatment of the film in a gas of the missing component. Another option would to fabricate the film through evaporation from a premixed target, instead of sputter deposition. This evaporation synthesis would be usable for the finalized LSC with optimal composition, since evaporating from a single target leads to a film that is homogenous in composition.

The excellent color rendering indices (R_a > 90), neutral CCT between 5000 and 6000 K, and lack of self-absorption make that Tm-doped halide LSCs can find use in the built environment as large scale LSCs, when covered with a suitable sealant.

CRediT authorship contribution statement

Evert P.J. Merkx: Conceptualization, Methodology, Software, Validation, Formal analysis, Investigation, Data curation, Writing - original draft, Writing - review & editing, Visualization. **Maarten P. Plokker:** Investigation, Writing - review & editing. **Erik van der Kolk:** Conceptualization, Writing - review & editing, Supervision, Project administration, Funding acquisition.

Declaration of competing interest

The authors declare that they have no known competing financial interests or personal relationships that could have appeared to influence the work reported in this paper.

Acknowledgments

The authors would like to acknowledge Vasilii M. Khanin for the fruitful discussions and the careful proofreading of the manuscript. This work was supported by the Netherlands Organization for Scientific Research (NWO/OCW) as part of the LumiCon project (15024).

Appendix A. Supplementary data

Supplementary material related to this article can be found online at https://doi.org/10.1016/j.solmat.2020.110944.

Detailed derivation of the relation between photoluminescent quantum yield and the mean decay time, representative EDX spectrograms, method used to determine the molar absorption coefficients of rare-earth-doped thin-film libraries.

Research data for this article

http://dx.doi.org/10.4121/uuid:bb8869cd-008b-4f84-bf82-e20c43e79509.

References

[1] European Union, Directive 2010/31/EU of the European Parliament and of the Council of 19 May 2010 on the energy performance of buildings (recast), Off. J. Eur. Union (ISSN: 17252555) (2010) 13–35.

[2] R.A. Ferreira, S.F. Correia, A. Monguzzi, X. Liu, F. Meinardi, Spectral converters for photovoltaics – What's ahead, Mater. Today (ISSN: 13697021) 33 (March) (2020) 105–121, http://dx.doi.org/10.1016/j.mattod.2019.10.002.

[3] E.P.J. Merkx, E. van der Kolk, Luminescent solar concentrators, in: M. Freunek (Ed.), Indoor Photovoltaics, first ed., Wiley-Scrivener, ISBN: 9781119605591, 2020, (Chapter 6).

[4] P. Moraitis, G. van Leeuwen, W. van Sark, Visual appearance of nanocrystal-based luminescent solar concentrators, Materials (ISSN: 19961944) 16 (6) (2019) http://dx.doi.org/10.3390/ma12060885.

[5] Y. Zhao, R.R. Lunt, Transparent luminescent solar concentrators for large-area solar windows enabled by massive Stokes-shift nanocluster phosphors, Adv. Energy Mater. (ISSN: 16146832) 3 (9) (2013) 1143–1148, http://dx.doi.org/10.1002/aenm.201300173, URL: http://doi.wiley.com/10.1002/aenm.201300173,

[6] Y. Zhao, G. Meek, B. Levine, R. Lunt, Near infrared harvesting transparent luminescent solar concentrators, Adv. Opt. Mater. 2 (7) (2014) 606–611, URL: http://onlinelibrary.wiley.com/doi/10.1002/adom.201400103/full.

[7] C. Yang, M. Moemeni, M. Bates, W. Sheng, B. Borhan, R.R. Lunt, High-performance near-infrared harvesting transparent luminescent solar concentrators, Adv. Opt. Mater. (ISSN: 2195-1071) 8 (8) (2020) 1901536, http://dx.doi.org/10.1002/adom.201901536, URL: https://onlinelibrary.wiley.com/doi/abs/10.1002/adom.201901536.

[8] E.P.J. Merkx, O.M. ten Kate, E. van der Kolk, Rapid optimization of large-scale luminescent solar concentrators: evaluation for adoption in the built environment, Opt. Express (ISSN: 1094-4087) 25 (12) (2017) A547–A563, http://dx.doi.org/10.1364/OE.25.00A547.

[9] E.P.J. Merkx, T.G. Lensvelt, E. van der Kolk, Modelling and optimization of UV absorbing photovoltaic windows using a thin film AlN:Eu^{3+} luminescence library, Sol. Energy Mater. Sol. Cells (ISSN: 09270248) 200 (June) (2019) 110032, http://dx.doi.org/10.1016/j.solmat.2019.110032,

[10] T.A. Cohen, T.J. Milstein, D.M. Kroupa, J.D. MacKenzie, C.K. Luscombe, D.R. Gamelin, Quantum-cutting Yb^{3+}-doped perovskite nanocrystals for monolithic bilayer luminescent solar concentrators, J. Mater. Chem. A (ISSN: 2050-7488) 7 (15) (2019) 9279–9288, http://dx.doi.org/10.1039/C9TA01261C, URL: http://xlink.rsc.org/?DOI=C9TA01261C.

[11] M. de Jong, W. Kesteloo, E. van der Kolk, Deposition of luminescent NaCl:Tm^{2+} thin films with a Tm concentration gradient using RF magnetron sputtering, Opt. Mater. (ISSN: 09253467) 46 (2015) 149–153, http://dx.doi.org/10.1016/j.optmat.2015.03.061.

[12] O.M. ten Kate, K.W. Krämer, E. van der Kolk, Efficient luminescent solar concentrators based on self-absorption free, Tm^{2+} doped halides, Sol. Energy Mater. Sol. Cells (ISSN: 09270248) 140 (2015) 115–120, http://dx.doi.org/10.1016/j.solmat.2015.04.002.

[13] P. Moraitis, R. Schropp, W. van Sark, Nanoparticles for luminescent solar concentrators - A review, Opt. Mater. (ISSN: 09253467) 84 (August) (2018) 636–645, http://dx.doi.org/10.1016/j.optmat.2018.07.034, URL: https://linkinghub.elsevier.com/retrieve/pii/S0925346718304944.

[14] E. Beurer, J. Grimm, P. Gerner, H.U. Güdel, Absorption, light emission, and upconversion properties of Tm^{2+}-doped $CsCaI_3$ and $RbCaI_3$, Inorg. Chem. 45 (24) (2006) 9901–9906, http://dx.doi.org/10.1021/ic061340.

[15] E. Beurer, J. Grimm, P. Gerner, H.U. Güdel, New type of near-infrared to visible photon upconversion in Tm^{2+}-doped $CsCaI_3$, J. Am. Chem. Soc. (ISSN: 00027863) 128 (10) (2006) 3110–3111, http://dx.doi.org/10.1021/ja0567790.

[16] J. Grimm, E. Beurer, P. Gerner, H.U. Güdel, pconversion between 4f-5d excited states in Tm^{2+}-doped $CsCaCl_3$, $CsCaBr_3$, and $CsCaI_3$, Chem. Eur. J. (ISSN: 09476539) 13 (4) (2007) 1152–1157, http://dx.doi.org/10.1002/chem.200600418.

[17] J. Grimm, J. Suyver, E. Beurer, G. Carver, H. Gudel, Light-emission and excited-state dynamics in Tm^{2+}-doped $CsCaCl_3$, $CsCaBr_3$, and $CsCaI_3$, J. Chem. Phys. 110 (5) (2006) 2093–2101.

[18] J. Grimm, O. Wenger, K. Krämer, H. Güdel, 4f–4f and 4f–5d excited states and luminescence properties of Tm^{2+}-doped CaF_2, $CaCl_2$, $SrCl_2$ and $BaCl_2$, J. Lumin. (ISSN: 00222313) 126 (2) (2007) 590–596, http://dx.doi.org/10.1016/j.jlumin.2006.10.007.

[19] J. Grimm, E. Beurer, H.U. Güdel, Crystal absorption spectra in the region of 4f4f and 4f5d excitations in Tm^{2+}-Doped $CsCaCl_3$, $CsCaBr_3$, and $CsCaI_3$, Inorg. Chem. (ISSN: 0020-1669) 45 (26) (2006) 10905–10908, http://dx.doi.org/10.1021/ic051951m.

[20] J. Grimm, H.U. Güdel, Five different types of spontaneous emission simultaneously observed in Tm^{2+} doped $CsCaBr_3$, Chem. Phys. Lett. (ISSN: 00092614) 404 (1–3) (2005) 40–43, http://dx.doi.org/10.1016/j.cplett.2005.01.051.

[21] M.P. Plokker, E. van der Kolk, Temperature dependent relaxation dynamics of luminescent NaX:Tm^{2+} (X=Cl, Br, I), J. Lumin. (ISSN: 00222313) (2019) http://dx.doi.org/10.1016/j.jlumin.2019.116694.

[22] J.C. de Mello, H.F. Wittmann, R.H. Friend, An improved experimental determination of external photoluminescence quantum efficiency, Adv. Mater. (ISSN: 0935-9648) 9 (3) (1997) 230–232, http://dx.doi.org/10.1002/adma.19970090308.

[23] A. Rogora, G. Scudo, B. Ferrari, D. Testa, Luminescent, transparent and colored, PV systems in architecture: Potential diffusion and integration in the built environment, in: 30th International Plea Conference, CEPT University, 2014.

[24] T. Mansencal, M. Mauderer, M. Parsons, N. Shaw, K. Wheatley, S. Cooper, J.D. Vandenberg, L. Canavan, K. Crowson, O. Lev, et al., Colour, (0.3.15) 2020, http://dx.doi.org/10.5281/ZENODO.3627408.

[25] S. Westland, C. Ripamonti, Computational Colour Science Using MATLAB, John Wiley & Sons, Ltd, ISBN: 0470845627, 2004, http://dx.doi.org/10.1002/0470020326.

[26] G. Wyszecki, W.S. Stiles, CIE Method of calculating D-illuminants, second ed., Wiley, 2000.

[27] J.D. Fowlkes, J.M. Fitz-Gerald, P.D. Rack, Ultraviolet emitting $(Y_{1-x}Gd_x)_2O_{3-\delta}$ thin films deposited by radio frequency magnetron sputtering: Combinatorial modeling, synthesis, and rapid characterization, Thin Solid Films (ISSN: 00406090) 510 (1–2) (2006) 68–76, http://dx.doi.org/10.1016/j.tsf.2005.12.309,

[28] E.P.J. Merkx, E. van der Kolk, Method for the detailed characterization of cosputtered inorganic luminescent material libraries, ACS Comb. Sci. (ISSN: 2156-8952) 20 (11) (2018) 595–601, http://dx.doi.org/10.1021/acscombsci.8b00068.

[29] R. Alvarez, A. Garcia-Valenzuela, C. Lopez-Santos, F.J. Ferrer, V. Rico, E. Guillen, M. Alcon-Camas, R. Escobar-Galindo, A.R. Gonzalez-Elipe, A. Palmero, High-rate deposition of stoichiometric compounds by reactive magnetron sputtering at oblique angles, Plasma Process. Polym. (ISSN: 16128850) 13 (10) (2016) 960–964, http://dx.doi.org/10.1002/ppap.201600019.

[30] W.M. Haynes, D.R. Lide, T.J. Bruno (Eds.), CRC Handbook of Chemistry and Physics, 97, CRC Press, ISBN: 9781498754293, 2016.

[31] D.L. Smith, Thin-Film Deposition: Principles and Practice, McGraw-Hill Inc., (ISSN: 0009-4978) ISBN: 0070585024, 1996, http://dx.doi.org/10.5860/choice.33-3347.

[32] G. Blasse, B.C. Grabmaier, Luminescent Materials, ISBN: 0387580190, 1941, http://dx.doi.org/10.1038/148118b0.

[33] J.M.F. van Dijk, M.F.H. Schuurmans, On the nonradiative and radiative decay rates and a modified exponential energy gap law for 4f–4f transitions in rare-earth ions, J. Chem. Phys. (ISSN: 0021-9606) 78 (9) (1983) 5317–5323, http://dx.doi.org/10.1063/1.445485.

[34] S.J. Byrnes, Multilayer optical calculations, 2016.

[35] J. Wiegman, E. van der Kolk, Building integrated thin film luminescent solar concentrators: Detailed efficiency characterization and light transport modelling, Sol. Energy Mater. Sol. Cells (ISSN: 09270248) 103 (2012) 41–47, http://dx.doi.org/10.1016/j.solmat.2012.04.016.

[36] L. Desmet, A.J.M. Ras, D.K.G. de Boer, M.G. Debije, Monocrystalline silicon photovoltaic luminescent solar concentrator with 4.2% power conversion efficiency, Opt. Lett. (ISSN: 0146-9592) 37 (15) (2012) 3087–3089, http://dx.doi.org/10.1364/OL.37.003087,

[37] M.R. Bergren, N.S. Makarov, K. Ramasamy, A. Jackson, R. Guglielmetti, H. McDaniel, High-performance $CuInS_2$ quantum dot laminated glass luminescent solar concentrators for windows, ACS Energy Lett. (ISSN: 23808195) 3 (3) (2018) 520–525, http://dx.doi.org/10.1021/acsenergylett.7b01346.